Title	The effect of TiO2 and GeO2 composite mixing on the behavior of macroporous Li-Ion battery anode materials
Authors	Carroll, Aoife;Grant, Alex;Zhang, Yan;Gulzar, Umair;Douglas-Henry, Danielle;Nicolosi, Valeria;O'Dwyer, Colm
Publication date	2023-12-19
Original Citation	Carroll, A., Grant, A., Zhang, Y., Gulzar, U., Douglas-Henry, D., Nicolosi, V. and O'Dwyer, C. (2023) 'The effect of TiO2 and GeO2 composite mixing on the behavior of macroporous Li-Ion battery anode materials', Journal of the Electrochemical Society, 170(12), 120521(14pp). https://doi.org/10.1149/1945-7111/ad1371
Type of publication	Article (peer-reviewed)
Link to publisher's version	10.1149/1945-7111/ad1371
Rights	© 2023, the Authors. Published on behalf of The Electrochemical Society by IOP Publishing Limited. This is an open access article distributed under the terms of the Creative Commons Attribution 4.0 License (https://creativecommons.org/licenses/by/4.0/), which permits unrestricted reuse of the work in any medium, provided the original work is properly cited. - https://creativecommons.org/licenses/by/4.0/
Download date	2026-08-24 06:16:47
Item downloaded from	https://hdl.handle.net/10468/15828

OPEN ACCESS

The Effect of TiO_2 and GeO_2 Composite Mixing on the Behavior of Macroporous Li-Ion Battery Anode Materials

To cite this article: Aoife Carroll *et al* 2023 *J. Electrochem. Soc.* **170** 120521

Journal of The Electrochemical Society, 2023 **170** 120521

The Effect of TiO_2 and GeO_2 Composite Mixing on the Behavior of Macroporous Li-Ion Battery Anode Materials

Aoife Carroll,[1,2] Alex Grant,[1,2] Yan Zhang,[1,2] Umair Gulzar,[1,2] Danielle Douglas-Henry,[3,4] Valeria Nicolosi,[3,4] and Colm O'Dwyer[1,2,4,5,*,z]

[1]*School of Chemistry, University College Cork, Cork, T12 YN60, Ireland*
[2]*Micro-Nano Systems Centre, Tyndall National Institute, Lee Maltings, Cork, T12 R5CP, Ireland*
[3] *School of Chemistry, Trinity College Dublin, Dublin 2, Ireland*
[4]*AMBER@CRANN, Trinity College Dublin, Dublin 2, Ireland*
[5]*Environmental Research Institute, University College Cork, Cork T23 XE10, Ireland*

Highly ordered, macroporous inverse opal structures can be made as TiO_2/GeO_2 nanocomposites with various GeO_2 content and provide Coulombic and voltage stable response where the Ge content and its distribution influence the overall capacity at both slow and fast rates. These interconnected binder-free anodes were characterized using X-ray diffraction, high resolution transmission electron microscopy, selected area electron diffraction, energy dispersive X-ray spectroscopy and electron energy loss spectroscopy. The electrochemical response in half cells over 2000 cycles and various rates showed how the mixture affected key metrics for the material in battery cells. The data shows that a composite of intercalation and alloying compounds can provide good capacity (between theoretical maxima for either material alone) and excellent coulombic efficiency (>99%), even with low quantities of the higher capacity alloying compound. Compositional gradients or spatial heterogeneities in the distribution of one material in the composite are shown to affect capacity during cycling life, where a coulombically efficient increasing capacity is found as the higher capacity material becomes electrochemically active within the composite matrix as the material is modified during cycling.

 [DOI: 10.1149/1945-7111/ad1371]

Manuscript submitted October 4, 2023; revised manuscript received November 22, 2023. Published December 19, 2023.

Supplementary material for this article is available online

Lithium-ion batteries (LIB) have revolutionized the electronics and automotive industries, giving us wireless mobility for devices and clear, battery powered electric vehicles.[1] However, advancements in electronics and the need for long life and higher energy density EV batteries have led to a growing demand for more efficient, long-life lithium ion batteries (LIBs). While high energy density and fast charging times are beneficial, cost and safety also demand consideration. Subsequently, a lot of research has gone into developing novel battery materials capable of longer cycle life, materials that are scalable, cost effective, and with reduced dependence on critical raw materials. More recently, the focus on energy materials have involved significant efforts in nanostructured materials,[2,3] high entropy materials[4] and more sustainable compositions.[5] Looking at the anode side, intercalation mode materials such as graphite have been at the forefront of research and commercial batteries historically, with high quality graphite key to long lifetime cells based on NMC532 and NMC811 compounds.[6,7] Alloying type materials such as Si, Sn and Ge give very high capacity and are being introduced into manufacturing in modern LIB cells.[8–17] Much of the development in alloying electrodes, particularly silicon, deals with mitigating or minimizing deleterious effects of cycle volume expansion and contraction,[18] which requires specific material structures[19] and composites to form stable energy dense electrodes. However, for other alloying and intercalation materials, there are still some open questions related to their behavior and how composites of active materials can enhance overall anode response.

With this in mind, nano-structuring has been researched to accommodate this expansion as well as improve lithium diffusion in intercalation mode materials such as TiO_2.[20,21] In particular, 3D ordered macroporous materials (3DOM) such as inverse opal (IO) structures have gained considerable attention due to their promising features. Inverse opals are composed of interconnected pores and wall structures, resembling honeycomb, with nanometer-thick walls.[15] This organized structure brings with it benefits for electrochemical energy storage such as improved mass transport of lithium ions and electrons, enhanced electrolyte contact, better mechanical stability (preventing pulverization and cracking of conversion type materials) and higher energy density.[22–24] They are formed by infilling the void spaces inside a sacrificial opal template compared of an FCC arrangement of polystyrene (PS) spheres. These voids can be filled with a variety of materials such as metal oxides, polymers and semiconducting materials depending on the desired physical properties. Many recent efforts to define their response has shown that they provide stable and long-life cycling behavior at quite high specific current in the absence of conductive additive or binders.[25–29]

As an inexpensive, nontoxic, and abundant material, TiO_2 has become an attractive anode material that is useful in non-aqueous chemistries such as current Li-ion batteries, but also in aqueous rechargeable cells.[30,31] It limits cell performance and power due to a higher working potential compared to graphite, but it provides a similar working specific capacity and a structural integrity during battery cycling.[8] There are three main TiO_2 polymorphs that have been researched for use as anode materials: anatase, rutile and TiO_2-B, while amorphous TiO_2 has also been shown to be a promising candidate.[32,33] Anatase TiO_2 has the highest theoretical capacity of the crystalline phases, with 167 mAh g^{-1} in bulk form which corresponds to $Li_{0.5}TiO_2$, however with nanostructuring this has been shown to improve to upwards of 300 mAh g^{-1}.[34] However all polymorphs of TiO_2 deal with poor electrical conductivity and lower Li ion mobility, and to circumvent this issue composite materials have garnered significant interest in recent years.[8,35,36]

Compositing anode materials is also useful for dual-stage intercalation or for modifying/mitigating behaviors of one or other material at certain voltages, and for tuning overall capacity, conductivity, and other parameters. Silicon/titanium composites[37–40] have been shown to be useful due to silicon's high theoretical capacity (4200 mAh g^{-1}), and compounds containing germanium, which has a higher electrical conductivity (100 times higher than silicon) as well as faster lithium diffusivity (400× faster than silicon) show stable response.[41,42] It is still not clear how specifically the composites interact with alloying and how

*Electrochemical Society Member.
[z]E-mail: c.odwyer@ucc.ie

the ratio of composite materials improves overall electrode material behavior. With a theoretical specific capacity of 1623 mAh g^{-1}, germanium anodes also offer the potential of increased energy density.[43] Nevertheless, germanium is an alloying type anode and so deals with volume expansion issues, as well as this, pure Ge can be expensive to produce and so limits its scalability. However, previous reports have shown that by manufacturing GeO_2 (which is more cost effective) into an inverse opal structure, a high specific capacity can be obtained that is similar that of pure Ge.[44]

In this report, we describe the formation of highly ordered inverse opal nanocomposites of TiO_2 and GeO_2. We compare the effect of each oxide by investigating the electrochemical performance of two ratios of the material with higher volume fractions of GeO_2, a 2:1 TiO_2/GeO_2 inverse opal material and a 5:1 TiO_2/GeO_2. Structural characterization in the form of X-ray diffraction (XRD) and Raman spectroscopy shows some crystalline content as anatase TiO_2 and hexagonal GeO_2, while localized atomic resolution analysis such as selected area electron diffraction (SAED) show the material is largely amorphous. X-ray photoelectron spectroscopy (XPS) indicates the material is composite of the individual oxides and depth profiling reveals elemental Ge within the structure. The electrochemical performances of both materials are analyzed by cyclic voltammetry (CV), galvanostatic cycling (GCPL) and rate testing. We demonstrate that the TiO_2/GeO_2 IOs offer significantly increased capacities and improved capacity retention compared to pure TiO_2 previously reported.[45] The dual-phase IO electrode will be shown to be coulombically efficient after the initial cycles and remains so for over 2000 cycles. Unlike pure TiO_2 and GeO_2 IO electrodes, these composites exhibit a specific capacity that increases with cycle life between the 150th and 1000th cycles due to changes in reversible reactions and is followed by a more severe fading of specific capacity up to 2000 cycles. These reactions are coulombically efficient (>99%) allowing Li-ions to access metalloid Ge deeper beneath the surface.

Experimental

Materials preparation.—The substrates used were stainless steel (SS) discs (grade 304) with a diameter of 15.5 mm. The opal template was fabricated using the evaporation induced self-assembly (EISA) method, which involved suspending the SS discs in a 0.1% solution of polystyrene spheres (500 nm diameter) and deionized water and placing in a convection oven at 60 °C overnight.

A 0.1 M solution of titanium(IV) chloride tetrahydrofuran ($TiCl_4$.2THF) was prepared in IPA and a solution of 0.05 M germanium ethoxide ($Ge(OC_2H_5)_4$) was also prepared in IPA. These solutions were mixed in equal volumes to yield a molar ratio of Ti:Ge of 2:1 and in a 2.5:1 v/v to yield a molar ratio of Ti:Ge of 5:1. The dried PS sphere templates were then infilled by drop casting a volume of ~30 μl of the mixed precursor. The samples were then calcined at 450 °C for 1 h.

Material characterization.—SEM analysis was performed on FEI Quanta 650 FEG high resolution SEM at an accelerating voltage of 20 kV. EDS analysis of atomic composition was performed on FEI Quanta 650 FEG high resolution SEM at an accelerating voltage of 20 kV whilst EDS mapping was performed on Zeiss Supra 40 high resolution SEM at an accelerating voltage of 20 kV. Raman scattering was performed on an Ocean Optics QE65PRO Raman Spectrometer using a 20 mW Ar^+ laser at 532 nm excitation. The laser beam was focused onto the samples using a 40× objective lens and spectra were collected using a CCD camera. XPS spectra were acquired using a Kratos AXIS ULTRA spectrometer. Survey scans were recorded between 0 and 1486 eV with a step size of 1.0 eV, dwell time of 50 ms, and pass energy of 160 eV and 20 eV for narrow spectral regions. Core level scans were acquired with a step size of 0.05 eV, dwell time of 100 ms, and pass energy of 20 eV averaged over 10 scans with an analysis nominal area of ~220 μm^2. A non-monochromated Al Kα X-ray source at 300 W power was used for all scans. Data was processed using CasaXPS software where a Shirley background correction was employed, and peaks were fitted to Voigt profiles. For depth profiling, Ar^+ sputtering was in GCIS mono mode, at an energy of 5 keV and a 1.5 mm raster. X-ray diffraction (XRD) was conducted using a Philips X'pert Pro MPD, equipped with a Panalytical Empyrean Cu X-ray tube and a Philips X'celerator detector.

Transmission Electron Microscopy (TEM) was performed using a FEI Titan 80–300 ThermoFisher Scientific at 300 kV. Images were recorded using a Gatan UltraScan CCD camera. Selected Area Electron Diffraction (SAED) was done to evaluate crystallinity in the samples while elemental composition was determined by Energy Dispersive X-ray Spectroscopy (EDS) using a Bruker XFlash 6–30 EDS detector. Mapped regions were imaged in Scanning Transmission Electron Microscopy (STEM) mode with an angle annular dark-field (HAADF) detector. EDS spectrum analysis was done using Bruker Esprit 2.0. Electron Energy Loss Spectroscopy (EELS) was performed using a Tridium 863 spectrometer with the energy dispersion set to 0.1 eV/channel.

Electrochemical characterization.—All electrochemical characterization was performed using a BioLogic VMP3 Potentiostat/Galvanostat. The TiO_2/GeO_2 IOs were investigated in a half-cell configuration against a pure Li counter electrode, using a stainless-steel PAT-cell from El-Cell in a two-electrode configuration. The electrolyte used was lithium hexafluorophosphate solution, in ethylene carbonate and diethyl carbonate, 1.0 M $LiPF_6$ in EC/DEC = 50/50 (v/v), battery grade from Sigma Aldrich. The separator used was glass microfiber from Whatman Grade GF/A cut to size. The stainless steel discs were used as the current collector. The typical mass loading of the electrodes was 0.4–0.7 mg. All electrochemical tests were investigated in a potential window of 3.0 V—0.01 V. Cyclic voltammetry was performed at a scan rate of 0.1 mV/s for both ratios and galvanostatic cycling was preformed using various specific currents as mentioned in this report (75 mA g^{-1}–450 mA g^{-1}).

Results and Discussion

Structure and composition of TiO_2/GeO_2 composite inverse opals.—The TiO_2/GeO_2 inverse opal samples were prepared by evaporation induced self-assembly, then infilled with either the 2:1 ratio or the 5:1 ratio of the mixed precursor. The samples were annealed at 450 °C which led to the formation of the inverse opal structure which can be seen in Figs. 1a, 1b for the 2:1 ratio and Figs. 1c, 1d the 5:1 ratio. A highly ordered macroporous structure was formed in both cases with data in Supplementary material, Fig. S1 showing average pores diameters of ~406 nm for the 2:1 ratio, and ~412 nm for the 5:1 ratio, consistent with the slightly smaller value compared to the parent PS sphere due to volume expansion of the liquid crystallizing into the final inorganic composite oxide. Alternating layers comprising the inverse structure of the (111)- face centered cubic (fcc) sphere packing arrangement of the colloidal crystal template are visible in the pores of the IO. This interconnected 3D macroporous structure has been shown to allow for faster overall lithiation into nanoscale walls of the active phase in binder-free electrodes, infilled throughout with the electrolyte phase, and the porosity allows for the walls of the IO to expand into the empty pores.

EDS mapping was carried out to identify the atomic percentage and to establish the spatial distribution of Ti and Ge. Below are the EDS maps for each ratio with the corresponding picture shown without the mapping overlay, Figs. 1e and 1f display the 2:1 ratio and the 5:1 ratio, respectively, with related spectra in Supplementary material, Fig. S2. Both Ge and Ti appear to be distributed evenly within the material, not in isolated regions. XRD patterns for both composites prepared on stainless steel substrates were obtained (Fig. 1g). The reflections observed in both ratios can be readily indexed to both anatase TiO_2 (JCPDS No. 21–1272) and hexagonal

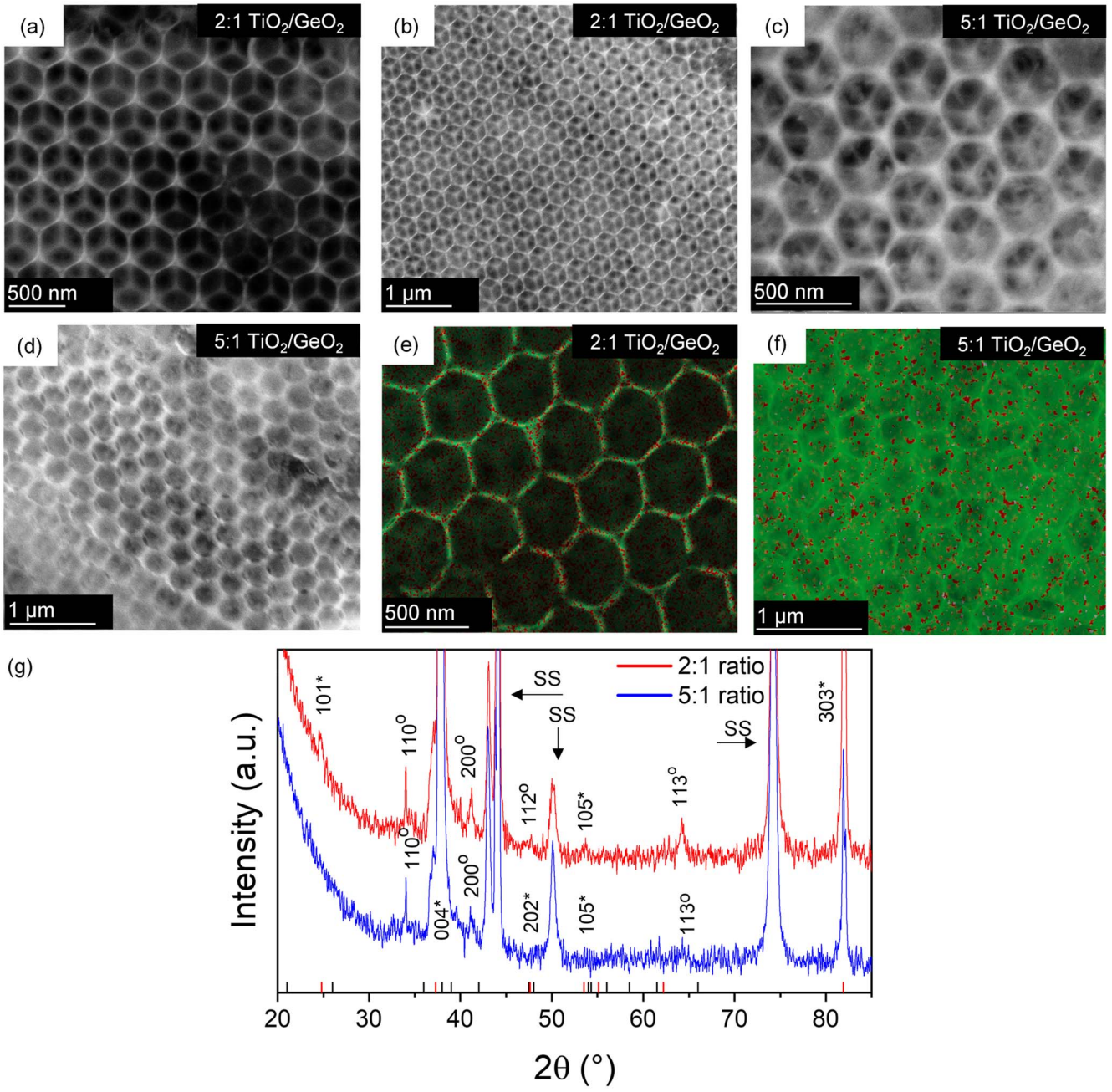

Figure 1. SEM images of TiO_2/GeO_2 inverse opals in (a), (b) 2:1 ratio and (c), (d) 5:1 ratio IOs. EDS elemental mapping of (e) 2:1 ratio and (f) 5:1 ratio with Ti depicted in green and Ge in red. (g) XRD patterns of both materials prepared on stainless steel. Reflections observed for stainless steel are denoted by SS while reflections labelled with * are from TiO_2 and reflections labelled with ° are from GeO_2.

GeO_2 (JCPDS No. 00–036–1463). The most predominant reflection observed for TiO_2 is the (004) reflection. For the 5:1 ratio, this is the most intense peak in relation to the other planes observed for anatase TiO_2, but show both forms of the composite have well crystallized phases.[46] For the 2:1 ratio, the other reflections (105), (101) and (303) are higher in intensity relative to the 5:1 ratio. The reflections observed for hexagonal GeO_2 which are (110), (200), (112) and (113) are seen with similar relative intensity in the 2:1 ratio. These reflections are diminished in appearance for the 5:1 ratio, as expected. The large peak for the (004) reflection from TiO_2 could possibly contain the (110) and (102) reflections from hexagonal GeO_2, however are difficult to detect due to the small deviance in reflectance angle.

Raman spectroscopy was performed on both ratios and on anatase TiO_2 and hexagonal GeO_2 inverse opals individually to compare, shown in Fig. 2. There are six active fundamental modes in anatase TiO_2 (A_g^1, 2 B_g^1 and 3 E_g), and a further 12 Raman active modes in hexagonal GeO_2 (4 A_g^1 and 8 E_g).[47,48] For the 2:1 TiO_2/GeO_2 material, Fig. 2a, peaks are observed at 172.6 cm^{-1}, 232.9 cm^{-1}, 257.5 cm^{-1}, 306.4 cm^{-1}, 417.6 cm^{-1}, 503.4 cm^{-1}, 617.0 cm^{-1}, 669.0 cm^{-1}, and 823.4 cm^{-1}. The highest intensity peak at 669.0 cm^{-1} matches well with the longitudinal optical (LO) E_g mode of hexagonal GeO_2. The peak beside this at 617.0 cm^{-1} is attributed to the E_g mode of anatase TiO_2, the proximity of these two peaks may be the cause of the high intensity when compared to the other peaks. The peaks recorded at 232.9 cm^{-1}, 257.5 cm^{-1} and 823.4 cm^{-1} are the three A_g^1 modes present in the 2:1 ratio which are consistent with the peaks observed for hexagonal GeO_2 only. The peaks observed at 172.6 cm^{-1} corresponds to the E_g mode of anatase TiO_2 and the peak at 503.4 cm^{-1} can be assigned to the

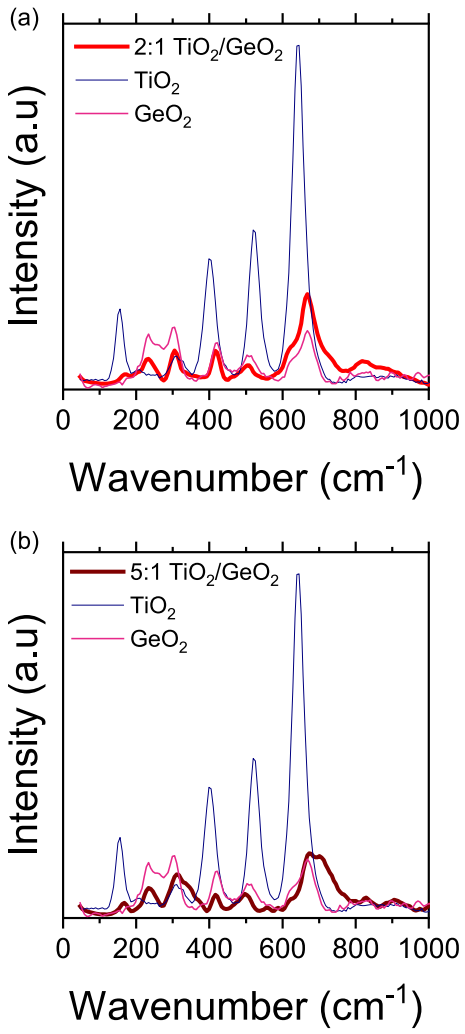

Figure 2. Raman spectra of (a) 2:1 ratio and (b) 5:1 ratio TiO_2/GeO_2 IOs overlayed with Raman spectra of anatase TiO_2 inverse opals (blue) and hexagonal GeO_2 inverse opals (pink).

characteristic split A_g^1 mode and B_g^1 mode of TiO_2. The peak at 417 cm^{-1} is difficult to assign due to the little variance in wavenumber of the A_g^1 mode of GeO_2 and the B_g^1 mode of TiO_2. The peak at 306.4 cm^{-1} can be attributed to the transverse optical (TO) phonon mode (E_g) of crystalline germanium, which indicates some metalloid of Ge is present throughout the structure.[44]

Figure 2b shows the Raman spectrum for the 5:1 TiO_2/GeO_2 IOs, compared to the phonon modes for single phase TiO_2 and GeO_2 in IO structure. The peaks observed are similar to that of the 2:1 spectrum, although some are slightly shifted. Nine peaks are initially recorded at 166.4 cm^{-1}, 237.4 cm^{-1}, 313.3 cm^{-1}, 375.4 cm^{-1}, 417.6 cm^{-1}, 497.3 cm^{-1}, 675.7 cm^{-1}, 698.8 cm^{-1} and 828.3 cm^{-1}. The peak at 237.4 cm^{-1} is attributed to the A_g^1 mode of hexagonal GeO_2 and can be deconvoluted to yield a second peak at 257.5 cm^{-1} also attributed to the A_g^1 mode. The third A_g^1 mode for hexagonal GeO_2 is found at 828.3 cm^{-1}, slightly blue shifted from the peak observed for the 2:1 ratio.

The largest peak centered at 692 cm^{-1} contains the doubly degenerate E_g mode for anatase TiO_2 (675.7 cm^{-1}) and hexagonal GeO_2 (698.8 cm^{-1}) both are observed at a longer wavenumber than recorded for the individual oxides and for the 2:1 ratio, this may indicate compression or shortened chemical bond lengths.[49] The peak assigned to the TO phonon mode (E_g) of crystalline germanium is observed at 313.3 cm^{-1} for the 5:1 ratio. The sharp peak at 417.6 cm^{-1} remains unchanged as seen for the 2:1 ratio however an additional peak is recorded at 375.4 cm^{-1} which is likely to be the B_g^1 mode of TiO_2, so the peak at 417.6 cm^{-1} may correspond to the A_g^1 mode of hexagonal GeO_2. The peak at 497.3 cm^{-1} can be assigned to the characteristic split A_g^1 mode and B_g^1 mode of TiO_2, red shifted from the peak observed for 2:1, which often indicates tensile strain within the crystal structure.

XPS was used to study the chemical states and electronic structure of the TiO_2/GeO_2 IOs, an initial scan was performed first and then depth profiling was carried out to analysis subsurface chemistry. The XPS spectra of the Ti 2p and 3p, Ge 2p and 3d and the O 1s core levels for the TiO_2/GeO_2 2:1 ratio and 5:1 ratio IO samples are presented in Fig. 3. The C 1s core level emission is shown in Supplementary materials, Fig. S3. The Ti 2p core-level photoemission for both ratios are very similar, consisting of two hyperfine split photoemission peaks at ~458.6, 464.3 eV for Ti $2p_{3/2}$ and Ti $2p_{1/2}$ with corresponding satellite peaks at 471.6 and 477.3 eV. The binding energies of these levels confirm that the Ti present in the IO samples correspond to Ti^{4+}.[50] The Ge 2p core-level spectra for both ratios are also similar, reading at 1219.7 eV for the 2:1 ratio and 1219.9 eV for the 5:1 ratio, and indicates Ge is present as Ge^{4+} in the form of GeO_2.[51] The Ge 3d spectra contain the Ge 3d and Ti 3p core level photoemission, and we see a noticeable difference between the two composite ratios. The Ge 3d peak is seen at 32.0 eV and can be readily assigned to GeO_2 and the Ti 3p peak has a binding energy of 37.1 eV which corresponds to TiO_2.

No other oxidation state other than +4 is observed for Ge or Ti and so the material primarily consists of a complex of both GeO_2 and TiO_2 nanoparticles arranged in an ordered interconnected macroporous lattice. For the 2:1 ratio the Ge 3d core-level has a higher relative intensity compared to the Ti 3p peak, however, this relative intensity switches to the Ti 3p peak for the 5:1 ratio, indicating more Ti 3p electrons in the 5:1 ratio than in the 2:1 ratio when compared to Ge 3d electrons. This is expected for the 5:1 ratio as the likelihood of the XPS beam probing a Ti-rich area is higher. The O 1s core levels for both ratios can be deconvoluted into two peaks and appear at the same binding energy values, one at 530.1 eV and the other at 531.5 eV. The peak at 530.1 eV is attributed to the Ti-O bond in TiO_2, while the peak at 531.5 eV corresponds to the O 1s for GeO_2, again indicating that the TiO_2/GeO_2 IO samples are a composite of TiO_2 and GeO_2, and from the overall XPS analysis, are stoichiometric +4 oxidation states of both Ti and Ge.[52]

Depth profiling was carried out on both ratios of IO composites by XPS to examine the subsurface chemistry. Figure 4 shows Ti 2p, Ge 2p, Ge 3d and O 1s core level spectra for both ratios after various Ar^+ sputtering times. In the Ti 2p spectrum for both ratios Ti $2p_{3/2}$ and Ti $2p_{1/2}$ spin–orbit split peaks are observed at binding energies of 458.8 eV, and 464.5 eV. Shoulder peaks are seen at 456.9 eV and 462.6 eV, which are shown to increase in area with depth as shown in Fig. S4.

The binding energy levels of 458.8 eV and 464.5 eV, which were also present in the initial scan are attributed to Ti^{4+} oxidation state for TiO_2 confirming the stoichiometric phase of the TiO_2. The 456.9 eV and 462.6 eV are artefacts of Ar^+ bombardment, causing localized reduction of the Ti^{4+} species to sub-oxide (Ti^{3+} oxidation state) often by O-vacancy formation.[53,54] The depth profiles of the Ti 2p core level of the 5:1 ratio composite shows a similar response, and the peaks remain largely unchanged with effects of Ar^+ somewhat more readily observed.

We also analyzed the Ge chemical state in each of the composites. The depth profile for the Ge 2p core level in Fig. 4b consists of two photoelectron emissions for both the 2:1 and the 5:1 ratio at the 30 s sputtering time. The peaks at ~1219 eV and ~1217 eV are attributed to the +4 oxidation state of germanium (GeO_2) and elemental Ge, respectively.[51] The detected concentration of elemental germanium increases with Ar^+ sputtering time as can be seen in Supplementary material, Fig. S4.

For the 2:1 ratio the concentration, at 30 s sputter time, of elemental Ge relative to Ge in a +4 oxidation state is 6.19% which increases to 21.8% at 700 s sputter time. For the 5:1 ratio the relative concentration of elemental Ge is 5.02% at 30 s sputter time,

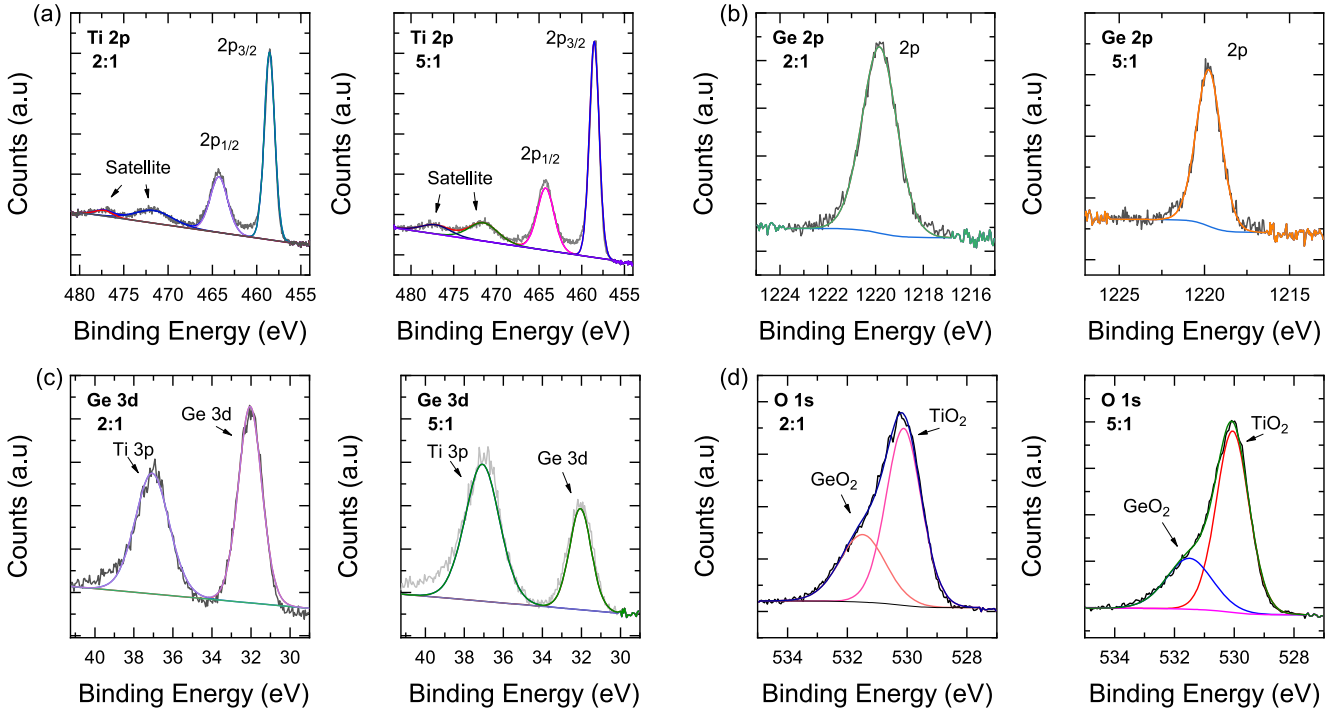

Figure 3. XPS analysis for 2:1 (left side) and 5:1 (right side) ratio of TiO_2/GeO_2 inverse opals of (a) Ti 2p (b) Ge 2p (c) Ge 3d, and (d) O 1s core level photoemission.

increasing to 18.72% at 700 s sputtering time. This is also observed in Fig. 4c the Ge 3d level, elemental Ge is not detected until 90 s sputter time, where it appears at a relative concentration of 10.90% for the 2:1 ratio, and 12.5% at the 5:1 ratio as shown in Supplementary material, Fig. S4. By 700 s sputtering time, this relative concentration increases to 24.71% for the 2:1 ratio and 24.56% for the 5:1 ratio. This implies elemental Ge is present deeper within the structure of the TiO_2/GeO_2 inverse opals. The O 1s depth profiles for both ratios are shown in Fig. 4d and consist of two deconvoluted peaks centered at 530.5 eV and 532 eV which correspond TiO_2 and GeO_2 respectively.

Localized atomic resolution analysis showed amorphous nature with some polycrystalline areas at nanoscale for the samples. Figures 5a and 5b show transmission electron microscopy (TEM) images of the inverse opal macrostructure for the 2:1 and 5:1 ratio respectively, and compared to the SEM images in Fig. 1, we can see the interconnected structure of the inverse opal in transmission. Interestingly, Figs. 5c and 5d show high resolution TEM images of the 2:1 ratio and the 5:1 ratio, respectively, which reveal the dominant amorphous nature of the material. Figures 5e and 5f show the selected area electron diffraction (SAED) for the 2:1 ratio composite for two areas of interest, (e) reveals elements of polycrystals with the (004), (105), (107), (200) and (204) planes being observed for anatase TiO_2 and the (011) and (200) plane for hexagonal GeO_2. However, Fig. 5f shows the SAED for the same sample indicating an amorphous region. Generally, these macroporous Ios are largely amorphous with localized regions of crystallinity on the nanoscale. Figure 5g shows the SAED for the 5:1 ratio, indicating its amorphous nature, no areas of polycrystals were found. Figure 5i shows a TEM image of the overlapping walls of the inverse opal structure of for the 2:1 ratio sample and the resulting EDX maps in Figs. 5j–5l of Ge, Ti and O confirm a relatively uniform spatial distributions of the three elements. A similar overall observation is made from measurement of the 5:1 composite ratio material in Figs. 5m–5p, showing a relatively homogenous mixture within the interaction volume of the electron beam. Pore diameters for the 2:1 ratio were measured at ~397 nm on average, which is in close agreement with the diameter found with SEM, while the pore diameters 5:1 ratio were found to be 457 nm on average (cf. Supplementary material, Fig. S1). The walls of the two materials appear to be made up of agglomerated nanoparticles and have varied thickness throughout ranging from 8–252 nm with an average of 85 nm for the 2:1 TiO_2/GeO_2 ratio while the walls of the 5:1 ratio of an average thickness of 63 nm, ranging from 17–239 nm.

Electron energy loss spectroscopy (EELS) showed no splitting of the $L_{2,3}$ edge which is common for crystalline TiO_2, and this splitting disappears in amorphous TiO_2 due to the lack of crowding from the octahedral site symmetry. A shift of 5 eV is observed when moving across the analysed region of the 2:1 ratio composite seen in Fig. S1, with the peak indicating the L_3 edge shifting from 464.4 eV to 460 eV and the Ti L_2 shifting from 470.2 eV to 465.4 eV across the sample area indicated by the orange bar. The oxygen K edge is also observed, recorded at 538.1 eV and shifted to 533.8 eV. The spectrum is in close agreement with the energy loss peaks observed by XPS for Ti^{4+}, the definitive peak without splitting indicates that the sample is predominantly amorphous TiO_2. Relatively little shift in Ti signal is observed for the 5:1 ratio, indicating no change in oxidation state for titanium.

Electrochemical behavior in long life Li-ion battery cells.— Cyclic voltammograms (CV) were acquired to investigate the Li^+ reaction mechanism for the TiO_2/GeO_2 inverse opals. The 1st, 2nd, 5th, and 10th CV scans for both composite ratios were acquired at a scan rate of 0.1 mV s^{-1} and are shown in Figs. 6a, 6b. For the 2:1 ratio in Fig. 6a, the broad shoulder centered at 1.9 V for the initial cathodic sweep can be attributed to the SEI layer formation, as it does not appear in subsequent cycles. The voltammetric current corresponding to SEI layer formation for the 5:1 ratio (Fig. 6b), also appears as a small shoulder centered at ~1.87 V. The peak at 1.2 V in Fig. 6a can be deconvoluted to give two reductions peaks, one at 1.26 V and 1.1 V. The peak at 1.26 V can be attributed to the lithium insertion into TiO_2 to yield Li_xTiO_2.[55] This can be seen to shift to a higher potential with subsequent cycles. The peak at 1.10 V corresponds to the formation of amorphous Li_xGeO_2.[56] In the 5:1 ratio, this peak appears more defined at 1.1 V, and was deconvoluted to contributions at 1.21 V for the lithium insertion into anatase TiO_2 (which is usually seen at a higher potential[57,58]) and 1.07 V for the

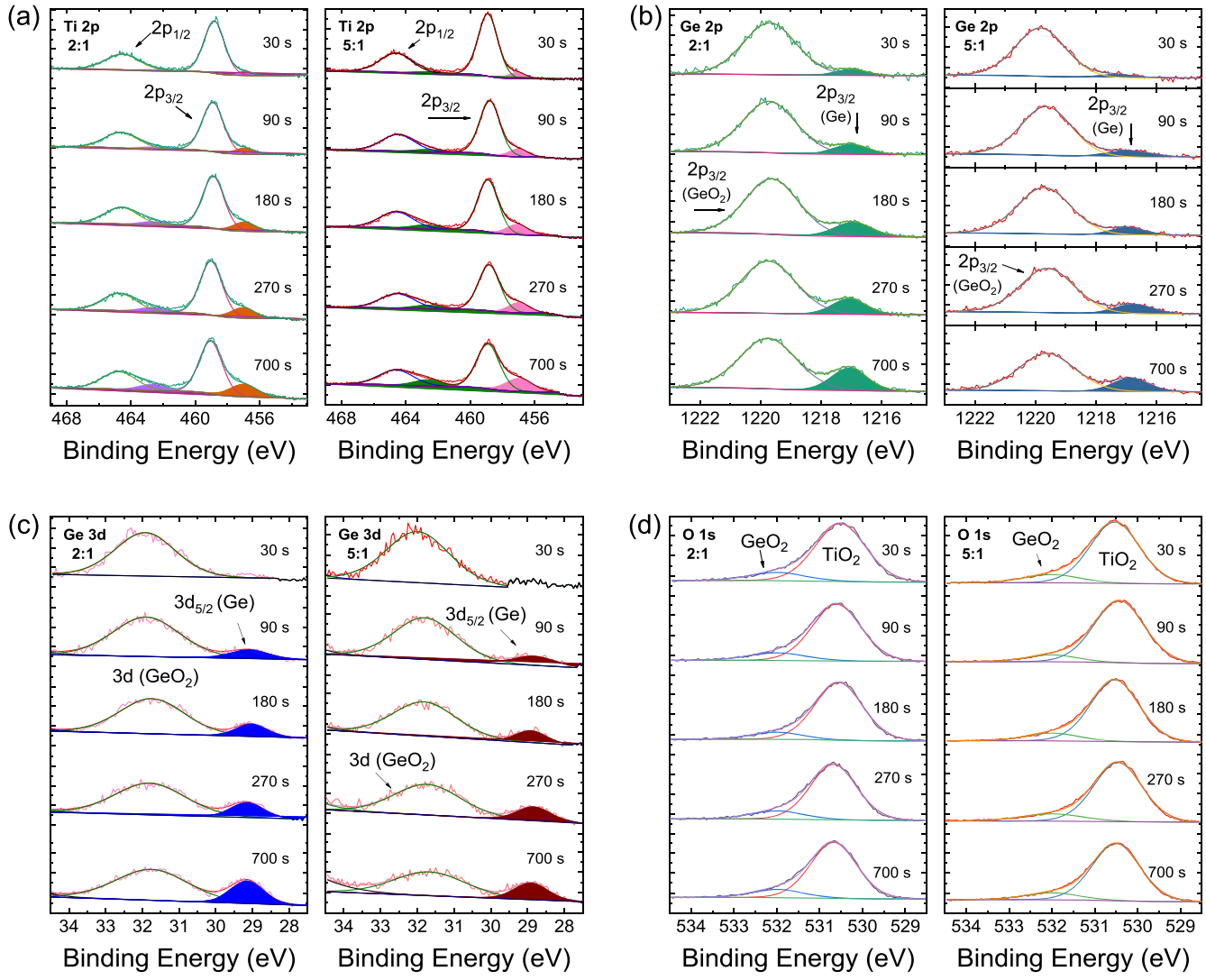

Figure 4. XPS depth profiles for (a) Ti 2p, (b) Ge 2p, (c) Ge 3d and (d) O 1s core levels for the 2:1 ratio and the 5:1 ratio of TiO_2/GeO_2 composite inverse opals. Ar^+ sputtering times were between 30 s and 700 s in each case at an energy of 5 keV with a 1.5 mm raster.

formation of amorphous Li_xGeO_2. The strong reduction peak at 0.7 V for the 2:1 ratio and 0.6 V for the 5:1 ratio may correspond to the decomposition of GeO_2 to Ge and the beginning of alloying with Li^+.[59] The sloping region in the cathodic scan from ~0.3 to 0.01 V for both ratios corresponds to the lithiation of crystalline Ge.[44,60]

For the anodic process, distinct voltage regions are observed for the 2:1 and 5:1 ratio of TiO_2/GeO_2 IOs. The first region is between 0.2–0.76 V for the 2:1 ratio, and 0.15–0.72 V for the 5:1 ratio, corresponding to the dealloying of $Li_xGe \rightarrow xLi + Ge$.[56,59] The peak observed at 1.1 V for both ratios is attributed to the oxidation of Ge/Li_2O to GeO_2, no shifts in voltage are seen in subsequent cycles indicating the reversibility of the lithiation/delithiation of GeO_2 in the compound.[61] The anodic peak observed for the delithiation of Li_xTiO_2 is seen at 2.02 V for the 2:1 ratio, and 1.98 V for the 5:1 ratio; this peak is typical for anatase TiO_2. A second, unusual peak is observed at 1.5 V, this has previously been observed for nanostructured TiO_2, however may not be present in bulk TiO_2 CVs.[58,62,63]

The lithium storage behavior of the mixed ratio inverse opals was investigated by galvanostatic cycling. Figures 6c and 6d show the discharge/charge profiles for the first hundred cycles for the 2:1 TiO_2/GeO_2 IOs and the 5:1 TiO_2/GeO_2 IOs respectively. Initial discharge capacities were recorded as 1994 mAh g^{-1} for the 2:1 and 1665 mAh g^{-1} for the 5:1 ratio, and the corresponding charge capacities were 1100 mAh g^{-1} and 1060 mAh g^{-1}, all at 150 mA g^{-1} specific current. For the 2:1 ratio there were four distinct regions observed: (1) a steep voltage drop from OCV to 1.5 V, which corresponds to the insertion into the tetragonal anatase lattice (Li_xTiO_2) and the formation of the SEI layer, (2) a sloping region from 1.5–1.0 V where it has been reported that in this region the Li-rich orthorhombic $Li_{0.5}TiO_2$ forms, (3) a sloping region from 1.0–0.8 V, which is credited to the formation of amorphous Li_xGeO_2 followed by a plateau at 0.8 V from the reduction of Li_xGeO_2 and GeO_2, and (4) the sloping region from 0.7–0.01 V attributed to the alloying of crystalline Ge with Li.[32,44,64] These regions are in excellent agreement with the cyclic voltammetry. The same regions are observed for the 5:1 ratio, however there is more distinction seen between regions in the voltage range of 1.5–0.8 V, a shorter plateau is observed between 1.5–1.2 V which has previously been reported as the lithium insertion into the orthorhombic anatase lattice, and decreased length of this plateau is linked to decreased particle size.[65] The voltage window for the formation of amorphous Li_xGeO_2 in both ratios seems to almost disappear in subsequent cycles, specifically after the 100th cycle. This implies that this reaction no longer occurs and the reversibility of the material cycling comes from the alloying and dealloying of Li with elemental Ge.[44] An interesting phenomenon is found to occur after 200 cycles that is characteristic for these composites IOs. In Fig. 6e for the 2:1 ratio

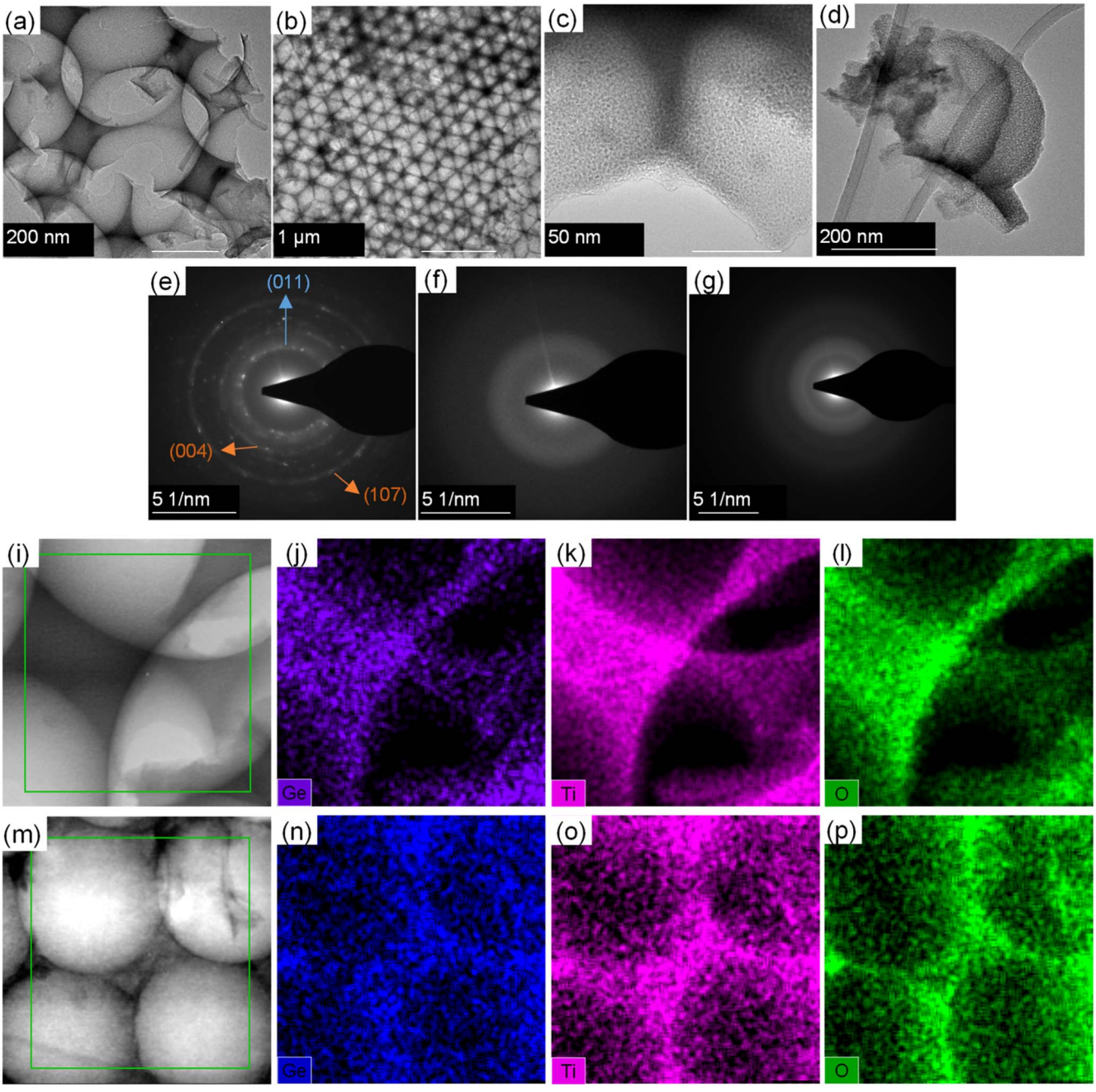

Figure 5. TEM images showing macro structure of inverse opals for (a) 2:1 TiO_2/GeO_2 and (b) 5:1 TiO_2/GeO_2. (c, d) HRTEM image showing amorphous nature at nanoscale for the 2:1 ratio and the 5:1 ratio respectively. (e) SAED pattern showing hints of crystallinity in the 2:1 ratio and (f) SAED pattern showing area of amorphousness for the same sample. (g) SAED showing amorphousness of the 5:1 ratio. (i) TEM image of 2:1 ratio showing an area of overlapping walls of the inverse opal structure and (j),(k) & (l) resulting EDX mapping showing the presence of Ge, Ti, O respectively. (m) TEM image of 5:1 ratio and corresponding EDX maps showing the presence of (n) Ge, (o) Ti, and (p) O.

and Fig. 6f for the 5:1 ratio, we observe with every 100 cycles or so, the specific capacity increases. For the 100th cycle the discharge capacity is 372 mAh g^{-1} for the 2:1 ratio, and 490 mAh g^{-1} for the 5:1 ratio of TiO_2/GeO_2 IOs. For the 2:1 ratio, which has a higher relative proportion of Ge content, the specific capacity after 200 cycles is 317 mAh g^{-1}, this increases to 360 mAh g^{-1} for the 500th cycle and then to ∼500 mAh g^{-1} by the 1000th cycle, a 58% increase in specific capacity from the 200th cycle. For the 5:1 the increase is found to occur earlier. After the 150th cycle the discharge capacity is 480 mAh g^{-1}, and by the 200th cycle we find a specific capacity ∼550 mAh g^{-1}, which continues to increase to reach ∼700 mAh g^{-1} for the 500th cycle and ∼730 mAh g^{-1} for the 1000th cycle. This equates to a 32% increase in capacity from the 200th cycle. In all cases, a coulombic efficiency >99% is maintained. This observation could have many possible causes,[66] including;

1. Volume expansion, contraction and pulverization happening during the first 100 or so cycles, which may expand the pores and open up new surface and allow better access to some of the higher specific capacity Ge content within the walls of the IO.
2. The region associated with the formation of Li_xGeO_2 is no longer observed after approximately 100 cycles and so the reversibility largely comes from the lithiation/delithiation of elemental germanium. The charge consumed forming this intermediate phase ceases and so a higher capacity is achieved.

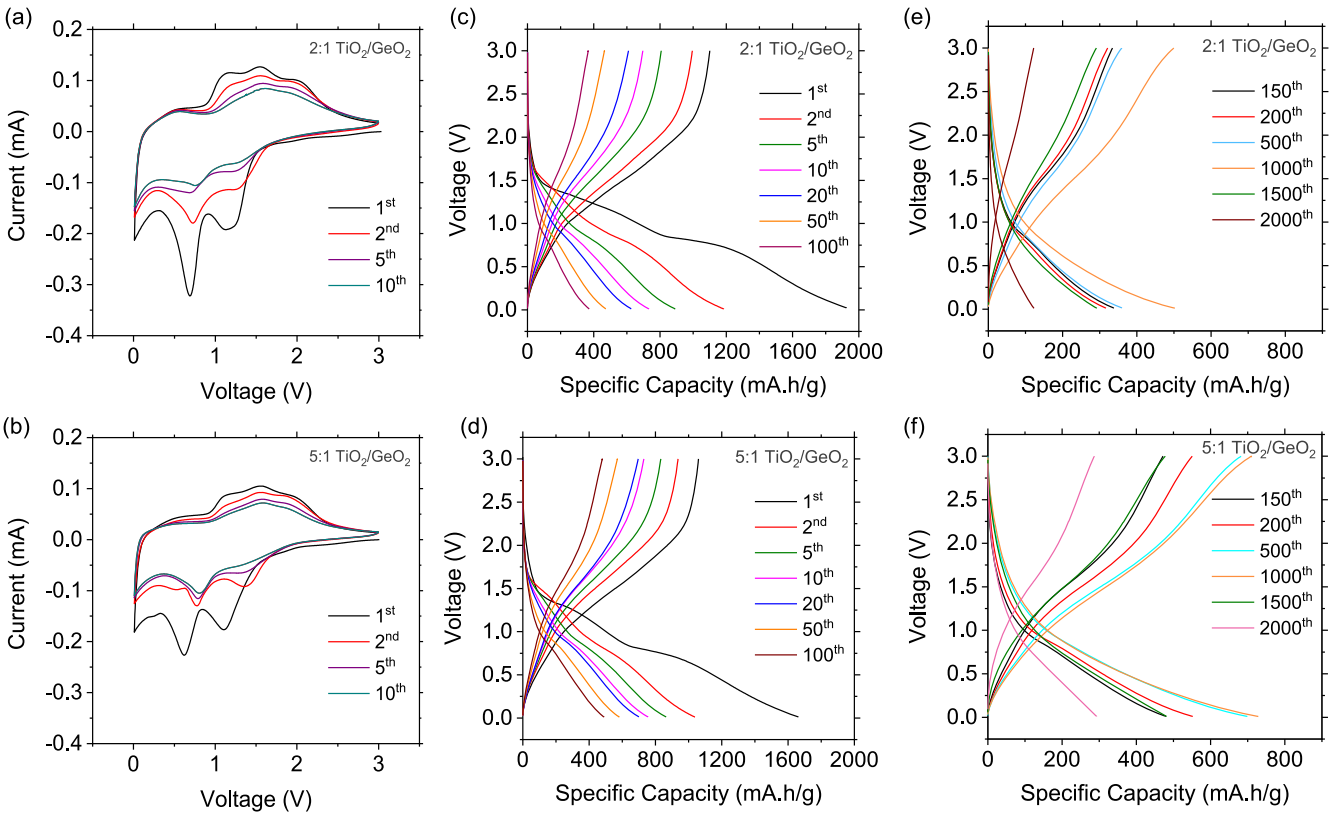

Figure 6. Cyclic voltammograms showing the 1st, 2nd, 5th, and 10th cycles for (a) the 2:1 ratio and (b) the 5:1 ratio of TiO_2/GeO_2 IOs. Discharge/charge profiles for 1st, 2nd, 5th, 10th, 50th and 100th cycles for (b) the 2:1 ratio and (c) the 5:1 ratio of TiO_2/GeO_2 IOs cycled at 150 mA g^{-1} specific current in a potential window of 3.00 − 0.01 V (vs Li/Li^+). Discharge/charge profiles for (e) the 150th, 200th, 500th, 1000th, 1500th and the 2000th cycles for (e) the 2:1 ratio and (f) the 150th, 200th, 500th, 700th, 900th and 1000th cycles for the 5:1 ratio.

3. More elemental Ge is accessed deeper within the structure (detected from XPS depth profiling), and with cycling, it is plausible that Li can access Ge in an oxidation state that allows a higher capacity contribution during cycling without prior reduction of Ge from its oxide, while not affecting the overall cycle coulombic efficiency.

After the 1000th cycle for the 2:1 ratio the capacity fades off rapidly falling to 292 mAh g^{-1} at the 1500th cycle (~60% loss in capacity), decreasing to 123 mAh g^{-1} after 2000 cycles. The 5:1 ratio by comparison, is better at retaining its capacity, with a specific capacity of 481 mAh g^{-1} after 1500 cycles which equates to a 34% loss in capacity from the 1000th cycle. Overall, a higher GeO_2 content does provide a capacity increase in the composite in general, but we see that in consistently coulombically efficient cycling, a reduction from a 1 part in 3 to 1 part in 6 of GeO_2 content behaves similarly and offers a scaled overall capacity based on the Ge content in the TiO_2/GeO_2 mixture, but the distribution of Ge and it accessibility during cycling has a strong influence on the capacity values during cycling.

Differential capacity plots (DCPs) were configured to better illustrate the phase transformations occurring in the first 200 cycles for both materials. Figure 7 shows the DCPs for the charge and discharge processes for the 2:1 and 5:1 ratio with the corresponding intensity maps for the cycle number. For the discharge process of the 2:1 ratio, and four regions are observed similar to those seen in the CVs, showing that Li insertion takes place over a number of steps. These peaks are seen at 1.5 V, 0.96 V, 0.8 V and a sloping region from 0.4 V—0.01 V. These peaks are associated with the reduction of TiO_2, the formation of amorphous Li_xGeO_2, the reduction of GeO_2 to crystalline Ge and the lithiation of crystalline Ge, respectively. The peaks associated with the transformation of TiO_2 to Li_xTiO_2 and the formation of amorphous Li_xGeO_2 no longer appear after the first few cycles and only those corresponding to the reduction of GeO_2 and lithiation of crystalline Ge are present. The same four regions are seen in the 5:1 ratio composite, appearing at 1.5 V, 0.94 V, 0.8 V and a sloping region from 0.4 V—0.01 V. The fading of charge contribution from TiO_2 is also present in the 5:1 ratio, highlighted in the intensity maps in Fig. 7.

For delithiation/charge process, four regions are observed: at 0.5 V, 1.1 V, 1.5 V and 1.9 V, for both ratios, for the delithiation of crystalline Ge, the oxidation of Ge to GeO_2 and two peaks associated with the delithiation of TiO_2. These peaks are in excellent agreement with those recorded for the cyclic voltammetry. The peak at 1.9 V that is attributed to the delithiation of TiO_2, fades after the first few cycles as seen in the discharge process. The peak observed at the highest intensity is the peak at 1.5 V, previously observed for nanostructured TiO_2 as mentioned and also for the lithium extraction mechanism for Ge.[67]

Coulombic efficiency during cycling was measured and can be seen in Figs. 8a and 8b together with the variation of specific capacity during cycling over ~2000 cycles. The consistent capacity increase over the first ~1000 cycles occurs after the material reaches its first stably reversible composition between 100–150 cycles. Prior to this, the capacity drops until it reaches a stable value, but the CE ~99% is always maintained in this material. The initial Coulombic efficiency (ICE) was ~57% and ~64% for the 2:1 ratio and the 5:1 ratio respectively. The low Coulombic efficiencies are limited to the first cycle and so are attributed to the formation of the SEI layer and Li_2O, low ICE has also been previously observed for Ge-based materials, but once the high CE state is reached the material, even in IO form, has been shown to cycle stably in previous investigations.[11,43,61]

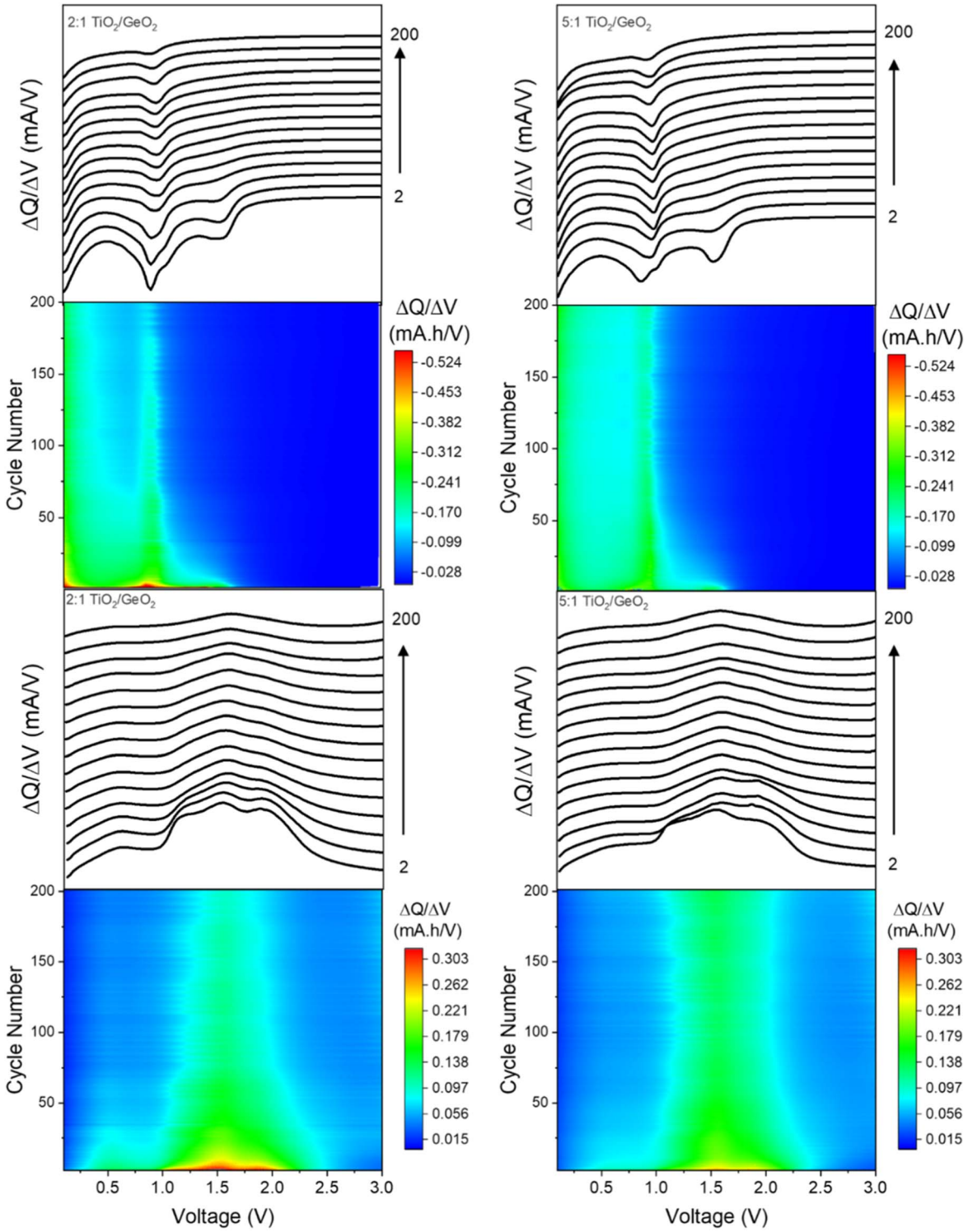

Figure 7. Differential capacity plots (DCP) and associated intensity maps for the charge and discharge states of the 2:1 TiO_2/GeO_2 IOs (left) and the 5:1 TiO_2/GeO_2 IOs (right).

As a composite, the 2:1 ratio shows excellent columbic efficiency, between 83% and 99% for the first 20 cycles and maintains an average CE of 99.8% for subsequent cycles. The 5:1 ratio displays better CE initially of >90% for the first 20 cycles and has an average CE of 99.8% for subsequent cycles. The monotonic increase in capacity due to reasons outlined earlier is relatively constant and once it reaches maximum, we then observe a decay in capacity in both composite ratios.

Rate capability tests were also conducted and can be seen in Fig. 8c. These tests involved charging and discharging the cell at various increasing specific currents ranging from 75–450 mA g^{-1}. Both ratios were cycled for 50 cycles at specific current of 150 mA g^{-1} prior to rate testing to eliminate SEI layer and side reactions and to obtain the composition with high (>99%) CE. The results are shown in Fig. 8c both ratios demonstrated excellent capacity retention and rate performance. The average discharge

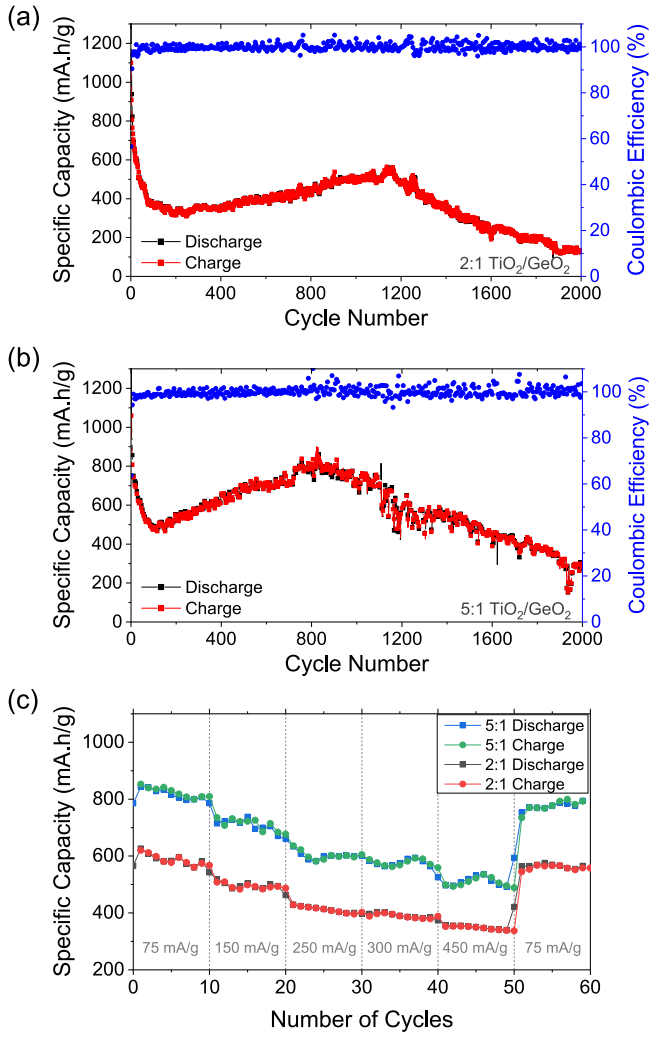

Figure 8. Coulombic efficiency graph showing charge and discharge plots at specific current of 150 mA g^{-1} for (a) 2:1 ratio of TiO_2/GeO_2 IOs and (b) 5:1 ratio of TiO_2/GeO_2 IOs. (c) Rate response test for both the 2:1 and 5:1 ratio with various specific currents.

capacity at the specific current of 75 mA g^{-1} was ~590 mAh g^{-1} for the 2:1 and ~920 mAh g^{-1} for the 5:1. This decreased to ~500 mAh g^{-1} and ~750 mA g^{-1} at specific current of 150 mA g^{-1} for the 2:1 and 5:1, respectively. The 2:1 ratio better retains its capacity for the 250 mA g^{-1} applied current, showing an average of ~420 mAh g^{-1} compared to the 5:1 which averaged at ~554 mAh g^{-1}. At specific current of 300 mA g^{-1} the capacity average was ~390 mAh g^{-1} (2:1 ratio) and ~500 mAh g^{-1} (5:1 ratio), this decreased slightly to ~350 mAh g^{-1} for the 2:1 ratio and ~440 mAh g^{-1} for the 5:1 ratio at a specific current of 450 mA g^{-1}. When the materials were cycled again at the initial specific current of 75 mA g^{-1}, the average specific discharge capacities were recorded as ~550 mA g^{-1} for the 2:1 and ~770 mAh g^{-1} for the 5:1 ratio, proving excellent capacity retention for both materials. The 2:1 ratio loses only 6.1% of its average specific capacity while the 5:1 ratio loses 16.5% of its specific capacity. These results highlight that these TiO_2/GeO_2 IO materials are capable of outstanding reversible capacity, with the 2:1 ratio displaying excellent capacity retention and the 5:1 composite ratio demonstrating that the specific capacity of TiO_2 can be increased with only a small amount of GeO_2.

From the rate capability tests, both composites of the IO materials are able to deliver significantly high capacities at high specific currents, and higher than those of pure TiO_2 or GeO_2 IO under similar conditions. Both the 2:1 and 5:1 TiO_2/GeO_2 samples were cycled at a specific current of 450 mA $g^{-1}$to further investigate the faster-rate performance. The results for these tests are shown in Fig. 9. The 2:1 ratio showed a high initial specific discharge capacity of 1406 mAh g^{-1} and the charge capacity was 796 mAh g^{-1}. The 5:1 ratio had an initial specific discharge capacity of 1633 mAh g^{-1}, comparable to the capacity observed at the specific current of 150 mA g^{-1}, the specific charge capacity was recorded as 793 mAh g^{-1}. This relates to a Coulombic efficiency of ~56% for the 2:1 ratio and ~49% for the 5:1 ratio during initial lithiation and delithiation. This low Coulombic efficiency is limited to the first cycle and again is attributed to reactions involving SEI formation. While the 5:1 initial capacity is higher, the 2:1 ratio displays better capacity retention at higher rates with the discharge capacities recorded after 100 cycles of ~475 mAh g^{-1} for the 2:1 ratio and ~410 mAh g^{-1} for the 5:1 ratio. These capacities are comparable to the values recorded at the slower rate and demonstrate that these materials can deliver exceptional performance at high rates.

Beyond the 100th cycle, an increase in capacity is observed again up to ~900 cycles with the 5:1 ratio exhibiting 398 mAh g^{-1} for the 150th cycle, increasing to 550 mAh g^{-1} for the 800th cycle, a 38% increase in capacity. The capacity was recorded as 538 mAh g^{-1} for the 1000th cycle and so an end to the increasing capacity is noted, consistent with other cells at lower rates in Fig. 6. Looking at the 2:1 ratio, an increase in capacity is again noted up until the 900th cycle. After 200 cycles the discharge capacity for the 2:1 ratio is ~510 mAh g^{-1} increasing to 670 mAh g^{-1} after 900 cycles, a 30% increase in specific capacity. Both composite IO ratio electrodes were stopped after 1000 cycles for the faster rate and so the final capacity for the 2:1 ratio was recorded at ~560 mAh g^{-1}. This is greater than the value recorded for the 5:1 ratio and to that seen for the 2:1 ratio at the lower rate of 150 mAh g^{-1}, which was ~500 mAh g^{-1}. This response may stem from the germanium dioxide which is known to perform well at high rates, including in IO macroporous form, and becomes electrochemically active later in the cycling life as the overall electrode material changes with cycling, as discussed earlier.[68] Figures 9e and 9f show the coulombic efficiencies recorded for the faster rate for the 2:1 ratio and the 5:1 ratio, respectively. The 2:1 ratio IO electrode shows stable coulombic efficiency with an ICE of 56% which is limited to the first cycle, and an average of 99.4% after that. The 5:1 ratio has a lower ICE of 48.6% and an average coulombic efficiency of 91.6% over the 1000 cycles. This is considerably lower than the 2:1 and also the CE recorded for the 5:1 ratio at the lower specific current of 150 mA g^{-1}.

As GeO_2 is a conversion/alloying type material, it is known to undergo a large volume change exceeding 300% while TiO_2 IOs have been shown previously to maintain their interconnected structure for over 5000 cycles with isotropic swelling.[11,45] The structural changes of the composite TiO_2/GeO_2 IOs after lithiation were studied using scanning electron microscopy (SEM), shown in Fig. 10, to investigate volume expansion and structural integrity. After 2000 cycles, the ordered IO structure in both ratios remains intact, although distorted. The 2:1 composite ratio pore diameters were measured to be ~330 nm, having shrunk ~20% in diameter from 406 nm before cycling. While the 5:1 ratio pores were measured to be ~350 nm, a 15% decrease from the 412 nm pore diameter measured before cycling. This is due to the swelling of the walls with lithium insertion which expand into the pores of the IO, helping to prevent pulverization of the overall structure. The interconnectivity of the porous structure is maintained however and while the periodic swelling has deformed the material over extended cycling, the electrolyte-accessible pore structure and the interconnectivity ensure that materials remain electrochemically active, evidenced by the CE and voltage profiles. SEM images taken after 1000 cycles at 450 mA g^{-1} for the 2:1 composite ratio and after the rate test for the 5:1 ratio are shown in supplementary material Figs. S6 and S7, respectively. These images show the

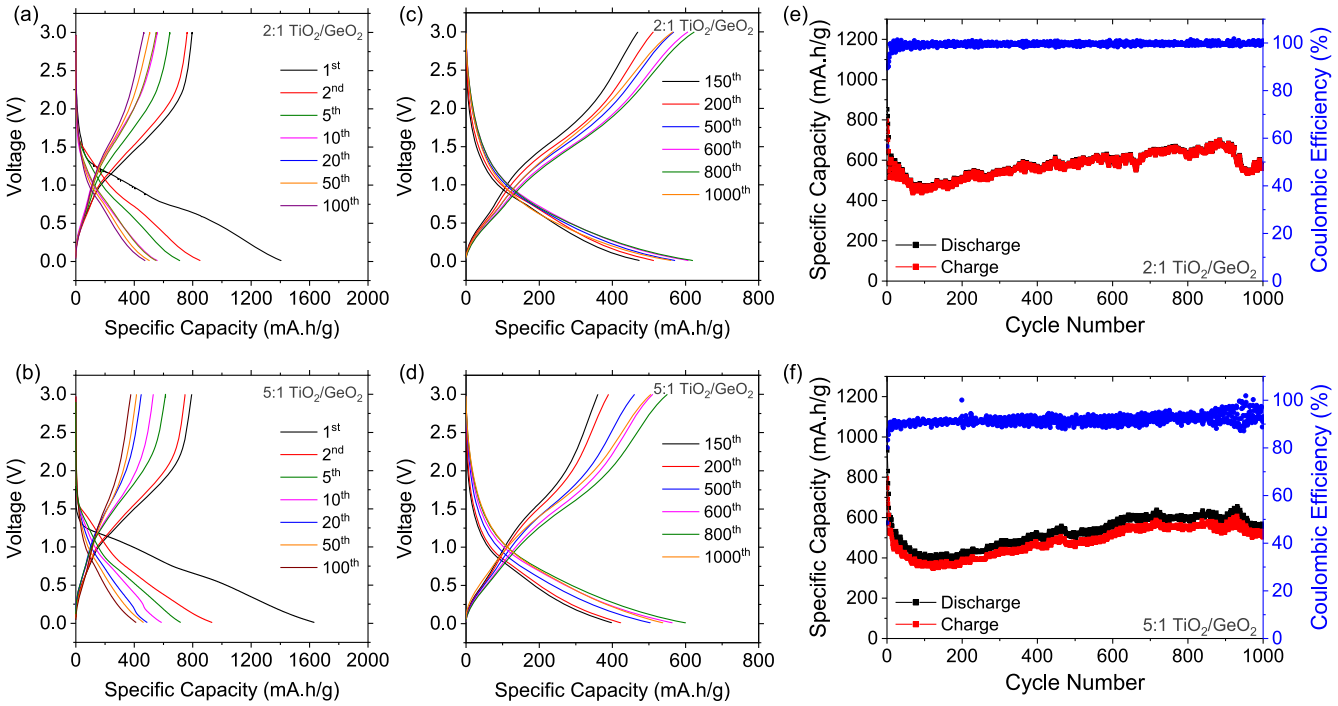

Figure 9. Charge and discharge plots at specific current of 450 mA g^{-1} for (a) 2:1 ratio of TiO_2/GeO_2 IOs for cycles 1–100. (b) 5:1 ratio of TiO_2/GeO_2 IOs for cycles 1–100. (c) 2:1 ratio of TiO_2/GeO_2 IOs for cycles 150–1000 and (d) 5:1 ratio of TiO_2/GeO_2 IOs for cycles 150–1000.

structural integrity, which is inherent to the inverse opal morphology, remains even with various current densities.

Conclusions

Highly ordered, macroporous inverse opal structures can be made as TiO_2/GeO_2 nanocomposites with various GeO_2 content and provide Coulombic and voltage stable response where the Ge content and its distribution influence the overall capacity at both slow and fast rates. Material characterization showed anatase TiO_2 and hexagonal GeO_2 phases. GeO_2 incorporation appears to be graded, and XPS identified more elemental Ge below the surface of the IO electrode material.

The introduction of relatively small amounts of germanium improves the specific capacity of TiO_2 with the 2:1 ratio having an initial specific capacity of 1994 mAh g^{-1} and the 5:1 ratio reaching 1665 mAh g^{-1} at a specific current of 150 mA g^{-1}. Both materials displayed interesting behavior between 200 and 900 cycles where we find a characteristic increase in specific capacities before capacity fading occurs in later cycles. This effect was linked to pulverization that opened fresh material to the electrolyte, including metalloid Ge, and a consistent reduction in the amount of GeO_2 with cycling, so that the charge contribution from its electrochemical reduction to elemental Ge reduced, prior to lithium alloying reaction. This effect is not seen in either pure TiO_2 or GeO_2 IO electrodes, and a unique observation for composites of these materials. The specific capacity of the 2:1 ratio composite IO increased by 58% from ~310 mAh g^{-1} at 200 cycles to ~500mAh g^{-1} for the 1000th cycle before fading to ~120 mAh g^{-1} by the 2000th cycle, having run for almost 10,000 h. The 5:1 ratio capacity increased from 480 mAh g^{-1} (150th cycle) to ~730 mAh g^{-1} (1000th cycle) which is a 52% increase before fading to ~330 mAh g^{-1} by the 1720th cycle, showing superior capacity retention when compared to the 2:1 ratio. While IO electrodes offer consistent and stable cycling behavior, this work identified features in composites that allow for capacity increases with cycling, while retaining coulombic efficiencies of >99% during this period of capacity increase. However, a maximum capacity is reached in all cases, followed by a more severe capacity fading than is normally seen in the pure TiO_2 and GeO_2 electrodes under similar conditions.

Rate testing was performed at intervals of 10 cycles with specific currents ranging from 75 mA g^{-1} to 450 mA g^{-1}. Both materials displayed good capacity retention, with the 2:1 composite ratio retaining 94% capacity while the 5:1 ratio retained 83.5% of its capacity. Dedicated fast rate cycling was performed at 450 mA g^{-1} for 1000 cycles with the 2:1 ratio exhibiting ~1400 mAh g^{-1} for the initial discharge, and ~1630 mAh g^{-1} for the 5:1 ratio. The 2:1 ratio IO behaved well under fast rate conditions displaying a reversible capacity of ~500 mAh g^{-1} with an average coulombic efficiency (CE) of 99.4%. For the 5:1 ratio displayed high capacity values (with a reversible capacity of ~400–500 mAh g^{-1}), the coulombic efficiency plot highlights issues with the average CE measured at 91.6%. Post cycling material characterization was done via SEM imaging and showed the structure is partially retained after 2000 cycles for the 2:1 ratio. These findings demonstrate that composites of well-behaved interconnected macroporous Li-ion battery anode materials exhibit unusual behavior even when coulombically efficient, and with stable and well-known voltage profiles. The accessibility and spatial distribution of the Ge is a key factor here, but difficult to control from solution mixing processes. Cycling does relieve this Ge content to become accessible and electrochemically active, with the results showing that a small Ge content has a significant influence on the behavior of the composite. An intriguing finding for dual phase composites such as these is that some reversible lithium reaction with the GeO_2 becomes self-limiting, and the system preferentially allows reversible alloying with metalloid germanium in the TiO_2/GeO_2 composites. In tandem, the capacity, once stabilized to >99% coulombic efficiency post-SEI formation, is seen to continually increase even with >99% efficiency, followed by a sharp fading of capacity with cycling. The data highlights some benefits of tailoring porous material and their compositions to improve capacity and rate-behavior, but also shows how sensitive and different reversible reactions can lead to efficient but variable specific capacities.

The data shows that a composite of intercalation and alloying compounds can provide good capacity and excellent coulombic efficiency, even with low quantities of the higher capacity alloying compound. Further, gradients from spatial heterogeneities are shown to affect capacity in cycling life, where increasing capacity are found

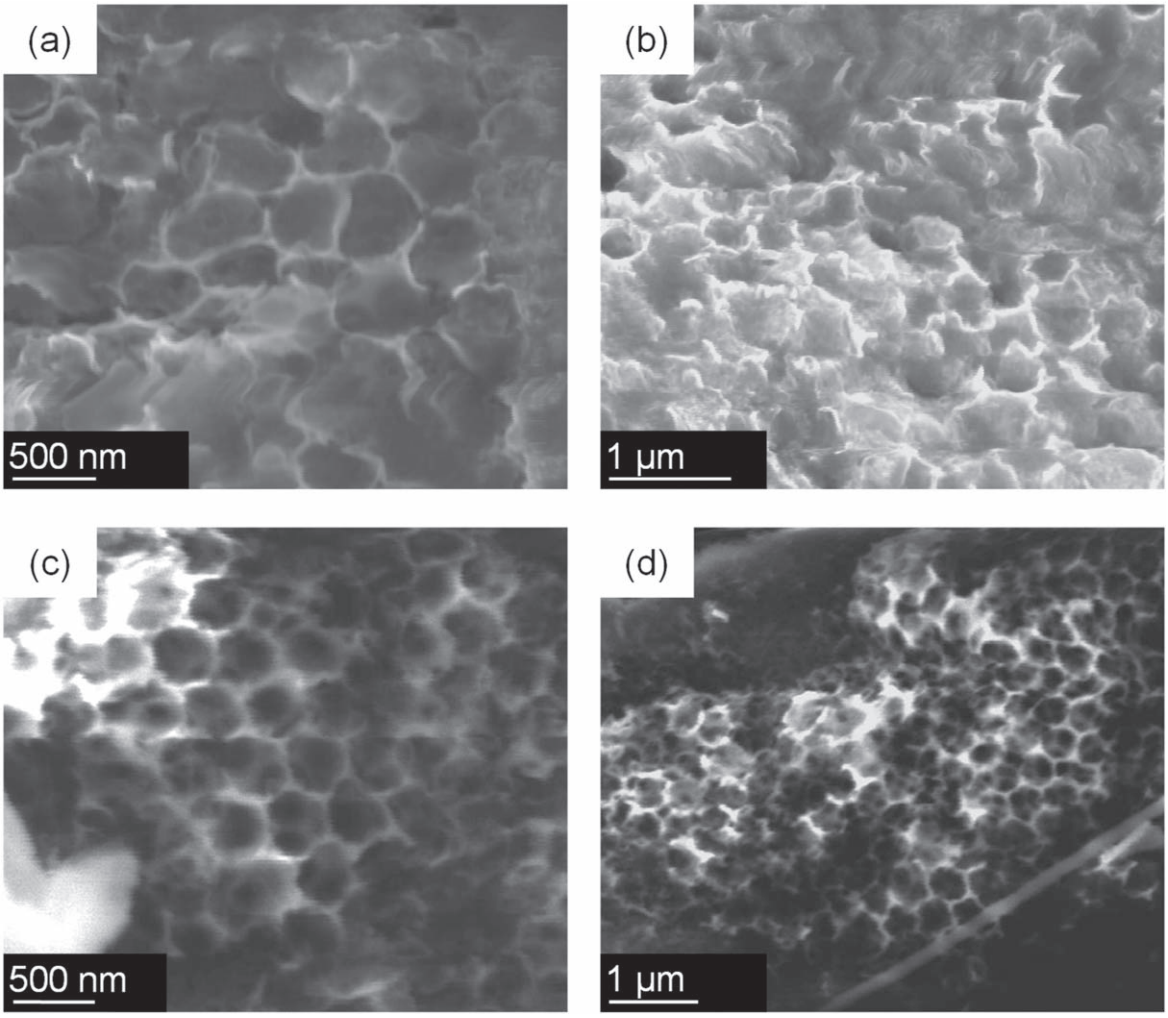

Figure 10. SEM images of (a), (b) the 2:1 TiO_2/GeO_2 IO material and (c), (d) the 5:1 TiO_2/GeO_2 IO material after 2000 cycles showing the interconnected pore structures. Volumetric swelling reduces the pore size. The fibrous material in some images are remnant glass fibers from the separators used in these cells.

as the higher capacity material is relieved within the composite matrix as the material is modified during cycling, while remaining ideally coulombically efficient. Composites using dissimilar Li reactions and the concentrations are potentially useful, but care is needed to ensure homogeneous formulation for cycling stability of the capacity values.

Acknowledgments

We acknowledge support from the Irish Research Council under an Advanced Laureate Award (IRCLA/19/118) and a Government of Ireland Postdoctoral Fellowship (GOIPD/2021/438). We also acknowledge support from the European Union's Horizon 2020 research and innovation program under grant agreement No. 825114. V. N. and D.D.-H. wish to acknowledge the support of the ERC CoG, 3D2DPrint (681544), SFI AMBER (12/RC/2278_P2) and SFI FFT R21/196. They would also like to acknowledge the SFI-funded CRANN Advanced Microscopy Laboratory (AML) for the provision of their facilities for the microscopy characterization and analysis.

ORCID

Colm O'Dwyer https://orcid.org/0000-0001-7429-015X

References

1. J. B. Goodenough and Y. Kim, *Chem. Mater.*, **22**, 587 (2010).
2. J. M. Tarascon and M. Armand, *Nature*, **414**, 359 (2001).
3. J. W. Choi and D. Aurbach, *Nature Reviews Materials*, **1**, 16013 (2016).
4. K. Wang et al., *Nat. Commun.*, **14**, 1487 (2023).
5. C. Bauer et al., *Nature Sustainability*, **5**, 176 (2022).
6. J. Harlow et al., *J. Electrochem. Soc.*, **166**, A3031 (2019).
7. A. Eldesoky, E. Logan, A. Louli, W. Song, R. Weber, S. Hy, R. Petibon, J. Harlow, S. Azam, and E. Zsoldos, *J. Electrochem. Soc.*, **169**, 010501 (2022).
8. J. Y. Liao and A. Manthiram, *Adv. Energy Mater.*, **4**, 1400403 (2014).
9. A. G. Dylla, G. Henkelman, and K. J. Stevenson, *Acc. Chem. Res.*, **46**, 1104 (2013).
10. Y.-Q. Wang, L. Gu, Y.-G. Guo, H. Li, X.-Q. He, S. Tsukimoto, Y. Ikuhara, and L.-J. Wan, *JACS*, **134**, 7874 (2012).
11. C. K. Chan, X. F. Zhang, and Y. Cui, *Nano Lett.*, **8**, 307 (2008).
12. K. H. Seng, M. H. Park, Z. P. Guo, H. K. Liu, and J. Cho, *Angew. Chem. Int. Ed.*, **51**, 5657 (2012).
13. U. Kumar Sen, A. Shaligram, and S. Mitra, *ACS Appl. Mater. Interfaces*, **6**, 14311 (2014).
14. Z. Q. Zhu, S. W. Wang, J. Du, Q. Jin, T. R. Zhang, F. Y. Cheng, and J. Chen, *Nano Lett.*, **14**, 153 (2014).
15. E. Armstrong and C. O'Dwyer, *J. Mater. Chem. C*, **3**, 6109 (2015).
16. E. Armstrong, D. McNulty, H. Geaney, and C. O'Dwyer, *ACS Appl. Mater. Interfaces*, **7**, 27006 (2015).
17. K. R. Phillips, T. Shirman, E. Shirman, A. V. Shneidman, T. M. Kay, and J. Aizenberg, *Adv. Mater.*, **30**, 1706329 (2018).
18. A. Mukhopadhyay and B. W. Sheldon, *Prog. Mater Sci.*, **63**, 58 (2014).
19. N. Liu, H. Wu, M. T. McDowell, Y. Yao, C. Wang, and Y. Cui, *Nano Lett.*, **12**, 3315 (2012).
20. Y. Zhang, Y. Tang, W. Li, and X. Chen, *ChemNanoMat*, **2**, 764 (2016).
21. D. Li, H. Wang, H. K. Liu, and Z. Guo, *Adv. Energy Mater.*, **6**, 1501666 (2016).
22. G. Collins, E. Armstrong, D. McNulty, S. O'Hanlon, H. Geaney, and C. O'Dwyer, *Sci. Technol. Adv. Mater.*, **17**, 563 (2016).
23. J. S. Sakamoto and B. Dunn, *J. Mater. Chem.*, **12**, 2859 (2002).
24. C. O'Dwyer, *Adv. Mater.*, **28**, 5681 (2016).
25. M. Osiak, H. Geaney, E. Armstrong, and C. O'Dwyer, *J. Mater. Chem. A*, **2**, 9433 (2014).
26. A. Lonergan and C. O'Dwyer, *Adv. Mater. Technol.*, **8**, 2201410 (2023).

27. D. McNulty, A. Lonergan, S. O'Hanlon, and C. O'Dwyer, *Solid State Ionics*, **314**, 195 (2018).
28. A. Vu, Y. Qian, and A. Stein, *Adv. Energy Mater.*, **2**, 1056 (2012).
29. H. Zhang, X. Yu, and P. V. Braun, *Nat. Nanotechnol.*, **6**, 277 (2011).
30. K. H. Reiman, K. M. Brace, T. J. Gordon-Smith, I. Nandhakumar, G. S. Attard, and J. R. Owen, *Electrochem. Commun.*, **8**, 517 (2006).
31. M.-S. Wu, M.-J. Wang, J.-J. Jow, W.-D. Yang, C.-Y. Hsieh, and H.-M. Tsai, *J. Power Sources*, **185**, 1420 (2008).
32. D. Dambournet, I. Belharouak, and K. Amine, *Chem. Mater.*, **22**, 1173 (2010).
33. F. Legrain, O. Malyi, and S. Manzhos, *J. Power Sources*, **278**, 197 (2015).
34. S. Liang, X. Wang, Y.-J. Cheng, Y. Xia, and P. Müller-Buschbaum, *Energy Storage Mater.*, **45**, 201 (2022).
35. Z. Wei, R. Li, T. Huang, and A. Yu, *J. Power Sources*, **238**, 165 (2013).
36. Q. Zhu, H. Hu, G. Li, C. Zhu, and Y. Yu, *Electrochim. Acta*, **156**, 252 (2015).
37. K. Chen, Y. Tan, Y. Gao, and Y. Y. Chen, *Electrochim. Acta*, **450**, 142165 (2023).
38. Y. Bai et al., *J. Power Sources*, **308**, 75 (2016).
39. M. Jiang, F. Zhang, G. Zhu, Y. Ma, W. Luo, T. Zhou, and J. Yang, *ACS Appl. Mater. Interfaces*, **12**, 24796 (2020).
40. E. M. Lotfabad, P. Kalisvaart, K. Cui, A. Kohandehghan, M. Kupsta, B. Olsen, and D. Mitlin, *Phys. Chem. Chem. Phys.*, **15**, 13646 (2013).
41. D. Wang, Y.-L. Chang, Q. Wang, J. Cao, D. B. Farmer, R. G. Gordon, and H. Dai, *JACS*, **126**, 11602 (2004).
42. G. H. Yue, X. Q. Zhang, Y. C. Zhao, Q. S. Xie, X. X. Zhang, and D. L. Peng, *RSC Adv.*, **4**, 21450 (2014).
43. L. C. Yang, Q. S. Gao, L. Li, Y. Tang, and Y. P. Wu, *Electrochem. Commun.*, **12**, 418 (2010).
44. D. McNulty, H. Geaney, D. Buckley, and C. O'Dwyer, *Nano Energy*, **43**, 11 (2018).
45. D. McNulty, E. Carroll, and C. O'Dwyer, *Adv. Energy Mater.*, **7**, 1602291 (2017).
46. Y. Pang, G. Xu, Q. Feng, J. Lv, Y. Qin, Y. Zhang, Z. Zheng, and Y. Wu, *Phys. Lett. A*, **382**, 2759 (2018).
47. H. C. Choi, Y. M. Jung, and S. B. Kim, *Vib. Spectrosc.*, **37**, 33 (2005).
48. J. F. Scott, *Physical Review B*, **1**, 3488 (1970).
49. G. H. Loechelt, N. G. Cave, and J. Menéndez, *J. Appl. Phys.*, **86**, 6164 (1999).
50. L. Pan, S. Wang, J.-J. Zou, Z.-F. Huang, L. Wang, and X. Zhang, *Chem. Commun.*, **50**, 988 (2014).
51. W. E. Morgan and J. R. Van Wazer, *J. Phys. Chem.*, **77**, 964 (1973).
52. D. McNulty, H. Geaney, Q. Ramasse, and C. O'Dwyer, *Adv. Funct. Mater.*, **30**, 2005073 (2020).
53. L. Hernan, J. Morales, L. Sanchez, J. L. Tirado, J. P. Espinos, and A. R. Gonzalez Elipe, *Chem. Mater.*, **7**, 1576 (1995).
54. U. Diebold, *Surf. Sci. Rep.*, **48**, 53 (2003).
55. V. A. Sugiawati, F. Vacandio, A. Galeyeva, A. P. Kurbatov, and T. Djenizian, *Front. Phys.*, **7**, 179 (2019).
56. L. Zeng, X. Huang, X. Chen, C. Zheng, Q. Qian, Q. Chen, and M. Wei, *ACS Appl. Mater. Interfaces*, **8**, 232 (2016).
57. S.-J. Bao, Q.-L. Bao, C.-M. Li, and D. Zhi-Li, *Electrochem. Commun.*, **9**, 1233 (2007).
58. L. Kavan, M. Grätzel, S. E. Gilbert, C. Klemenz, and H. J. Scheel, *JACS*, **118**, 6716 (1996).
59. S. Yan, H. Song, S. Lin, H. Wu, Y. Shi, and J. Yao, *Adv. Funct. Mater.*, **29**, 1807946 (2019).
60. C. R. Arro, A. T. I. Mohamed, and N. Bensalah, *Materials Today Communications*, **30**, 103151 (2022).
61. D. T. Ngo, R. S. Kalubarme, M. G. Chourashiya, C.-N. Park, and C.-J. Park, *Electrochim. Acta*, **116**, 203 (2014).
62. L. Kavan, J. Rathouský, M. Grätzel, V. Shklover, and A. Zukal, *J. Phys. Chem. B*, **104**, 12012 (2000).
63. B. Zachau-Christiansen, K. West, T. Jacobsen, and S. Atlung, *Solid State Ionics*, **28-30**, 1176 (1988).
64. V. Gentili, S. Brutti, L. J. Hardwick, A. R. Armstrong, S. Panero, and P. G. Bruce, *Chem. Mater.*, **24**, 4468 (2012).
65. M. Wagemaker, W. J. H. Borghols, and F. M. Mulder, *JACS*, **129**, 4323 (2007).
66. M. Jiang, J. Chen, Y. Zhang, N. Song, W. Jiang, and J. Yang, *Adv. Sci.*, **9**, 2203162 (2022).
67. L. P. Tan, Z. Lu, H. T. Tan, J. Zhu, X. Rui, Q. Yan, and H. H. Hng, *J. Power Sources*, **206**, 253 (2012).
68. X. Li, Z. Yang, Y. Fu, L. Qiao, D. Li, H. Yue, and D. He, *ACS Nano*, **9**, 1858 (2015).